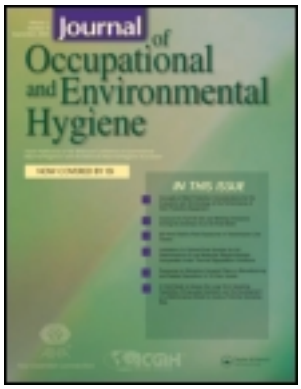

Journal of Occupational and Environmental Hygiene
Publication details, including instructions for authors and subscription information:
http://www.tandfonline.com/loi/uoeh20

Flow Dynamics and Contaminant Transport in Industrial-Type Enclosing Exhaust Hoods

Ertan Karaismail [a c], Ismail Celik [a] & Steven E. Guffey [b]

[a] Mechanical and Aerospace Engineering Department, College of Engineering and Mineral Resources , West Virginia University , Morgantown , West Virginia

[b] Industrial and Management Systems Engineering Department, College of Engineering and Mineral Resources , West Virginia University , Morgantown , West Virginia

[c] Currently with Rensselaer Polytechnic Institute , Scientific Computation Research Center Troy , New York

Accepted author version posted online: 01 Apr 2013.Published online: 22 May 2013.

To cite this article: Ertan Karaismail , Ismail Celik & Steven E. Guffey (2013) Flow Dynamics and Contaminant Transport in Industrial-Type Enclosing Exhaust Hoods, Journal of Occupational and Environmental Hygiene, 10:7, 384-396, DOI: 10.1080/15459624.2013.789749

To link to this article: http://dx.doi.org/10.1080/15459624.2013.789749

Journal of Occupational and Environmental Hygiene, 10: 384–396
ISSN: 1545-9624 print / 1545-9632 online

DOI: 10.1080/15459624.2013.789749

Flow Dynamics and Contaminant Transport in Industrial-Type Enclosing Exhaust Hoods

Ertan Karaismail,[1,*] Ismail Celik,[1] and Steven E. Guffey[2]

[1]Mechanical and Aerospace Engineering Department, College of Engineering and Mineral Resources, West Virginia University, Morgantown, West Virginia
[2]Industrial and Management Systems Engineering Department, College of Engineering and Mineral Resources, West Virginia University, Morgantown, West Virginia
[*]Currently with Rensselaer Polytechnic Institute, Scientific Computation Research Center, Troy, New York

The present study concerns the flow dynamics and associated contaminant transport in the near wake of a worker using an industrial-type benchtop enclosing hood. The primary focus is on evaluating the effects on the dynamics of the wake flow and the exposure level of various extraneous factors, such as the strength and direction of cross-drafts and the worker's body heat and shape. Three-dimensional Unsteady Reynolds-Averaged Navier-Stokes simulations were carried out for a model of a simple mannequin and a model of an anthropometric mannequin. Estimated flow patterns and concentrations near the simple mannequin were compared with the observations from concurrent smoke visualization experiments and with the experimental concentration measurements, respectively. Results for both visualizations indicated that the flow in front of the worker is dominated by dynamic vortical structures and that body heat may have negative effects on the exposure level, especially at low flow rates. Using simple rounded shapes to simulate the human form was a fair approximation from the viewpoint of flow structures and exposure trends, which agreed well with the experimental measurements and observations. However, the quantitative values of the predicted concentrations in the breathing zone were sensitive to the mesh resolution.

[Supplementary materials are available for this article. Go to the publisher's online edition of Journal of Occupational and Environmental Hygiene *for the following free supplementary resource: Figures S1–S11.]*

Keywords contaminant transport, enclosing exhaust hoods, wake flow

Correspondence to: Ertan Karaismail, Rensselaer Polytechnic Institute, Scientific Computation Research Center, 110 8th Street, Troy, NY 12180; e-mail: karaie@rpi.edu.

INTRODUCTION

Industrial-type enclosing exhaust hoods are widely used to protect workers from airborne contaminants generated while performing routine procedures. The transport of airborne contaminants into the breathing zone of the worker is highly associated with the airflow dynamics near the hood face. As the air enters the hood, the flow separates from the worker's body, leading to formation of unstable vortical flow structures and turbulence in the near wake.[1–7] These unstable flow structures can degrade the hood's effectiveness by carrying the airborne contaminants released in front of the worker into the worker's breathing zone. Hence, the larger the vortical structures, the more turbulent the wake. Due to the close relation between airflow dynamics and hood effectiveness, any factor that can affect the wake flow would also affect the hood's effectiveness. From the viewpoint of wake flow dynamics (the strength and direction of draft in a workplace), the worker's body heat and shape can be major factors. A good understanding of the combined and individual effects of these factors on the underlying airflow dynamics is essential for estimating exposure level control and the exhaust airflow necessary for effective hood performance.

Theoretically, enclosing exhaust hoods require a minimum face velocity to resist the disruptive effects of cross-drafts. It is reported that fume hoods should maintain an average face velocity of 0.4–0.6 m/sec (80–120 ft/min) with no face velocity measurement more than plus or minus 20% of the average.[8] However, the presence of the worker may introduce significantly low velocity regions at the hood face, thereby preventing uniformity of the hood face velocity. Furthermore, in many instances a high face velocity does not guarantee elimination of disruptive effects of the draft.[8,9] In particular, cases where high face velocities augment formation of eddies in the worker's wake can be problematic. This generally happens when the draft comes from the worker's back. For hoods with vertical face area, Zhivov et al.[10] showed that a moderate draft from behind the worker notably increases the concentration level in the worker's breathing zone. A detailed analysis of interactive effects of cross-drafts and face velocities was performed by Altemose et al.[1] for a laboratory-type hood with a horizontally sliding sash. The data collected indicated some outward leakage, mainly because of the unstable vortices

formed in the wake of the worker. Altemose and colleagues also reported that the temporal variation of the face velocity and magnitude of cross-drafts relative to face velocity are important variables in determining whether a hood with a sash will leak or not.

Understanding the thermal impact of the worker on wake flow is also fundamental to improving the design and operation of enclosing exhaust hoods. Unfortunately, the effect of buoyancy on the airflows associated with enclosing exhaust hoods has not been studied thoroughly. Nevertheless, the literature regarding the buoyancy driven flow about a human body in a quiescent or low wind speed indoor environment is numerous.[11–16] From these studies it is well known that in quiescent environments natural convection from the body to the surrounding air leads to the formation of a rising flow about the body (i.e., the human thermal plume).[11,13,16] However, when there is draft it becomes a forced-convection problem for which the addition of body heat dramatically changes the near wake flow pattern from two slowly recirculating eddies to a rising vertical plume. The latter produces velocities on the order of 0.1 m/sec, which can easily transport contaminants into the breathing zone from a nearby source.[17] In a recent numerical study, Li et al.[18] showed that the heat transfer from a worker's body may have a significant impact on the exposure level, especially when the convection induced by buoyancy dominates the flow.

The characteristics of wake flow also strongly depend on the worker's body shape. Since the body shape can vary significantly from person to person, it is not feasible to investigate the effects of all body shapes. The general approach in computational fluid dynamics (CFD) simulations as well as many experimental studies of such flows is to employ highly simplified body shapes, such as sharp-edged block body or a rounded body. Li et al.[18] investigated the effects of different body shapes on fluid flow and concentration patterns around the body in a wind tunnel and found that a sharp body or a block may not be good surrogates for the human form in occupational and environmental health studies.

This article focuses on the individual and combined effects of the aforementioned extraneous factors on the airflows and contaminant transport associated with industrial-type enclosing exhaust hoods. To our knowledge this issue has not yet been thoroughly addressed. The numerical predictions and experimental observations reported in this study contribute to the existing literature by providing insights into the effects of extraneous factors on the airflow pattern and contaminant transport in the near wake of a worker using an industrial-type benchtop enclosing hood.

EXPERIMENTAL SET-UP

For the visualization of airflow patterns inside the enclosing hood, smoke tests were performed in a wind tunnel that offers a working area of 4.92 m × 2.74 m × 3.66 m (length × height × width). A schematic representation of the wind tunnel and its contents are depicted in Figure 1. As can be seen, in the wind tunnel a mannequin and an experimental hood were employed to simulate a worker standing before an industrial-type enclosing exhaust hood. Both the hood face and the mannequin's shoulder-shoulder axis were positioned parallel to the draft, whose direction is indicated by the arrows. Unlike laboratory hoods, the working area of the hood was a rectangular box and did not have a sash. The dimensions of the enclosing hood were 0.91 m × 0.76 m × 1.14 m (width × height × depth). The top and right wall of the enclosing hood were made of Plexiglass to facilitate visualization experiments. The hood had a plenum section with a 95% opaque perforated plate to adjust the pressure distribution for a more uniform flow field at the hood face. It also had a 45° tapered take-off with a typical rectangular to round transition. The hood fan drew air through a circular duct connected to the 45° tapered take-off.

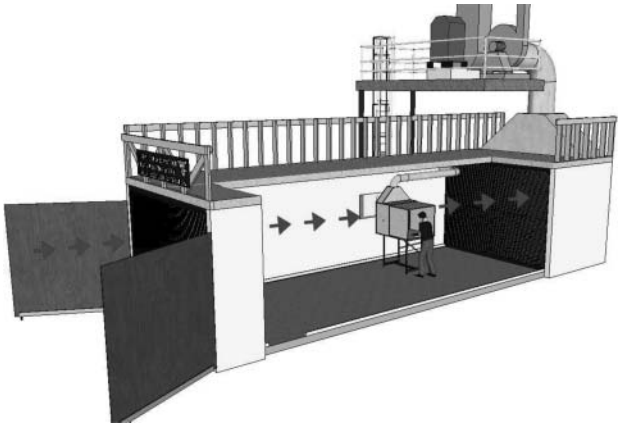

FIGURE 1. Schematic representation of the wind tunnel and its contents.

As shown in online Figure S1, two types of mannequins were used in the experiments. Mannequin A was an anthropometrically scaled male with hollow cavities in the head, torso, legs, and arms, as well as realistic facial features and short hair. It had heating coils producing 90 watts of power inside the torso to allow investigation of the effects of body heat. It was also clothed with loose-fitting pants and tucked-in t-shirt and was standing about 0.038 m away from the hood face. However, the head of the mannequin was partially inside the hood, breaking the plane of the hood face at its sideburns to simulate a realistic working condition. The "simple" Mannequin B on the other hand, consisted of a sphere, an elliptical cylinder (aspect ratio = 0.5) and two circular cylinders, representing the head, torso, and legs of a standing worker with arms resting on the sides, respectively. Both of the mannequins were 1.68 m high and had a shoulder width of 0.46 m. In the experiments, they were placed near the center of the width of the wind tunnel and in front of the hood with the center line on the symmetry plane of the hood.

In the flow visualization experiments, a tracer smoke was released upstream of the hood and mannequin so that it flowed with the cross-draft and was drawn into the hood by the suction

force created by the hood fan. In other cases, smoke was released from locations around the mannequin and the hood to better visualize localized phenomena. The transport of smoke pulled by the flow into the hood was recorded using a high-definition video camera for later review. The captured flow patterns were compared qualitatively with those estimated in the CFD simulations.

Also, in the experiments a total mass flow rate of 1.34×10^{-5} kg/sec of Freon 134a was released from a 0.23 m diameter, 0.05 m high cylindrical source placed on the work surface of the hood at 0.05 m from the face of the hood. The anthropometric mannequin's arms were extended forward in a "comfortable" position with its hands resting on the hood floor on either side of the tracer gas source. The simple mannequin had no arms. For assessment of exposure levels, the contaminant concentration in the breathing zone of the worker was sampled through the two ports, one adjacent to the nose and other near the mouth of the mannequin (online Figure S2). Further details of the experimental set-up can be found elsewhere.[19]

CFD MODEL

CFD simulations were performed to investigate the airflow and contaminant dispersion patterns inside the enclosing hood. For this purpose, a computational domain (Figure 2) representing the experimental configuration was generated using GAMBIT version 2.4.6 (ANSYS Inc., Canonsburg, Pa.), the commercial geometry and mesh generation software. Except for the length of the wind tunnel, the geometry matched the experimental configuration as closely as possible. The length of the computational domain was kept shorter than the actual length of the wind tunnel to minimize the artificial decay of turbulence specified at the inlet. The computational domain began approximately 2.25 m upstream of the hood.

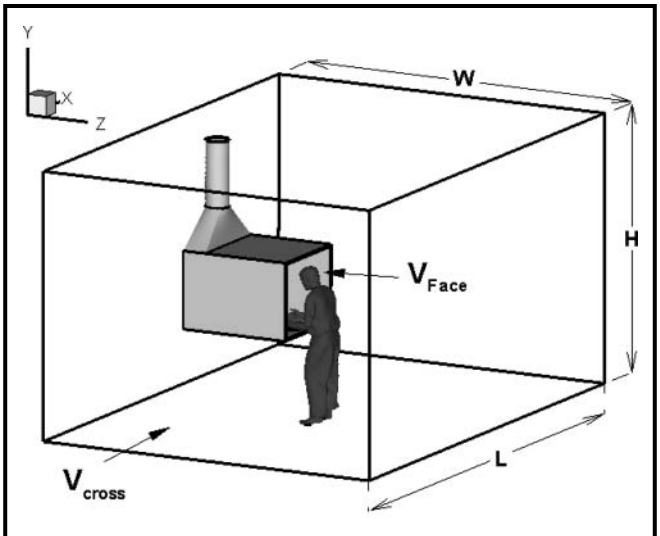

FIGURE 2. Computational domain.

In the simulations, the geometric models of both the anthropometric and rounded mannequins were used. The anthropometric mannequin, which will be called "humanoid," hereafter, was in a "working" position (i.e., its arms are reaching into the hood), unlike the simple rounded mannequin which represented a worker with arms resting on the sides. The geometric model of the humanoid was created using a laser scanner and the reverse engineering software, 3DReshaper version 5.0 (Technodigit SARL, Lyon, France). Accurately representing the highly curved shape of this manikin required a fine mesh. In this study, a mesh with 2,089,971 isotropic, tetrahedral elements was used. Online Figure S3 depicts the mesh structure on the mannequin and the hood surface.

Due to the high computational cost demanded by the fine mesh, the majority of the simulations were performed using the simple rounded mannequin. Simulations with the simple mannequin were performed on three different, non-uniform, unstructured meshes consisting of 518,101 (coarse mesh), 1,059,013 (medium mesh), and 1,181,922 (fine mesh) isotropic, tetrahedral elements. The main difference between the three meshes was the element density around the manikin. As with the mesh for the humanoid, for each mesh, finer elements were employed around the simple rounded mannequin and inside the hood to better resolve the flow in these critical regions. The range of meshes allowed assessment of the sensitivity of the numerical solutions to the mesh resolution.

Governing Equations and Boundary Conditions

In the present study, the flow was assumed to be incompressible, unsteady, and turbulent. In tensor notation, the URANS equations for the conservation of mass and momentum are written as follows:

$$\frac{\partial}{\partial x_i}(u_i) = 0 \tag{1}$$

$$\rho\left(\frac{\partial u_i}{\partial t} + u_j\frac{\partial}{\partial x_j}(u_i)\right) = -\frac{\partial p}{\partial x_i} + \frac{\partial}{\partial x_j}\left(\mu\frac{\partial u_i}{\partial x_j}\right) - \frac{\partial}{\partial x_j}(\rho\overline{u_i'u_j'}) + \rho_0 g\,(1-\beta\,(T-T_0)) \tag{2}$$

where u_i denotes mean velocity components. The fluctuating velocities are represented by u'_i and the overbar indicates time average. The mean pressure and the density are denoted by p and ρ, respectively. The gravitational force and the buoyancy force acting on the fluid are combined using the well-known Boussinesq approximation: $\rho = \rho_0(1-\beta\,(T-T_0))$ to eliminate ρ from the buoyancy term. In this term, which appears only in y-momentum equation, ρ_0 is the constant density of the flow, T_0 is the operating temperature, and β is the thermal expansion coefficient of the flowing medium at the operating temperature. The Boussinesq approximation is accurate as long as variations in actual density are small. Specifically, it is valid when $\beta(T-T_0) \ll 1$, a condition that holds for the present problem. The Reynolds stresses; $(\rho\overline{u_i'u_j'})$, appearing

on the right-hand side of the momentum equation (Eq. 2) were modeled using the RNG k-ε turbulence model.[20,21]

For simplicity, the contaminant (Freon 134a) released from the top surface of a cylindrical source placed on the hood floor was assumed to be a passive scalar that would not interfere with the flow. The passive scalar transport equation solved for the contaminant transport is given as:

$$\frac{\partial c}{\partial t} + \frac{\partial}{\partial x_j}(u_j c) = \frac{\partial}{\partial x_j}\left(\Gamma_m \frac{\partial c}{\partial x_j} - \overline{u'_j c'}\right) \quad \textbf{(3)}$$

where c and c' denote mean and fluctuating concentrations, respectively. Γ_m is the molecular diffusivity of the scalar quantity. Analogous to the turbulent momentum transport, the turbulent mass transport is approximated by the eddy-diffusivity concept;

$$\overline{u'_j c'} = \Gamma_t \frac{\partial c}{\partial x_j} \quad \textbf{(4)}$$

where Γ_t denotes the eddy (turbulent) diffusivity, and similar to the eddy (turbulent) viscosity (μ_t), it is not a fluid property but depends on the local state of turbulence. The Reynolds analogy between mass transport and momentum transport suggest that Γ_t and μ_t are closely related by the following relation:

$$\Gamma_t = \mu_t / Sc_t \quad \textbf{(5)}$$

where Sc_t is called the turbulent Schmidt number in mass transfer. The value of Sc_t is an important parameter since it determines how much the contaminant will diffuse. Experiments have shown that Sc_t for similar refrigerants (Freon 142b and 152a) are nearly constant, with typical values of 0.75.[22] In the present study, the value of Sc_t was chosen to be 0.7. However, in an attempt to test the sensitivity of the estimations to this parameter, Schmidt number of 1.0 was also used in the simulations. With the increased Schmidt number, the longtime-averaged concentration decreased about 8%.

The dominant mode of heat transfer from the worker's body to the surrounding air is mixed-convection. For this study, of particular interest are the conditions at which buoyancy effects are important. It is known that with increasing airflow rate the relative importance of buoyancy effects associated with natural convection decreases. However, the velocity range here is wide enough to expect significant buoyancy effects at some airflow velocities.

To account for the heat transfer from the worker's body to the air, the following equation for conservation of energy is solved:

$$\rho C_p \left(\frac{\partial T}{\partial t} + u_j \frac{\partial T}{\partial x_j}\right) = \frac{\partial}{\partial x_j}\left(k_{eff} \frac{\partial T}{\partial x_j}\right). \quad \textbf{(6)}$$

In Eq. 6, k_{eff} represents the effective thermal conductivity of the air, which is defined as the sum of molecular thermal conductivity k_m and turbulent thermal conductivity k_t ($= C_p \mu_t / \sigma_t$), where C_p is the specific heat at a constant pressure and σ_t is the turbulent Prandtl number.

As for the flow boundary conditions, fixed velocities based on the flow measurements were imposed at the hood and wind tunnel outlets. A zero pressure boundary condition was applied at the wind tunnel inlet. For all of the inlet and outlet boundary conditions, 10% turbulence intensity and a turbulent viscosity ratio of 10 were assumed. No-slip boundary conditions were imposed on the wind tunnel walls, hood walls, and the surface of the mannequin. The effects of the walls on turbulence were computed by the standard wall-function approach. For the passive scalar (contaminant) a total mass flow rate of 1.34×10^{-5} kg/sec with a turbulence intensity of 10% and turbulent viscosity ratio of 10 were specified on the top surface of the cylindrical contaminant source. At the walls, a zero normal gradient was imposed. At the hood and wind tunnel outlets, a zero stream-wise gradient boundary condition was used for the passive scalar. The porous jump boundary condition was used to model the 0.002 m thick perforated plate of the plenum which has about 16% area open to flow. A pressure jump coefficient of 3125 m^{-1} and a face permeability of 4×10^{-6} m^2 were used based on the pressure drop and velocity data obtained from a separate simulation of flow through the perforated plate. For the non-isothermal cases, constant temperature boundary conditions were imposed on the solid surfaces, including the mannequins. Based on the average temperatures measured in the experiments, the temperatures of the mannequin's head and neck were set to 300 K, and the shoulder and torso were kept at 303 K. The temperature for the mannequin's legs and the other walls were set equal to the air temperature (297 K). To match the experimental conditions heat was released only from the upper body of both of the mannequins.

Simulation Details

For the solution of the governing equations, a finite volume method (FVM) based commercial CFD software, FLUENT 6.3 (ANSYS Inc.) was used. The MUSCL scheme was used for spatial discretization of convective terms appearing in the passive scalar transport equation, and the second order upwind scheme was used for discretization of all other convective terms in other transport equations. All diffusive terms were discretized by the second order central differencing scheme. A first-order-accurate implicit scheme was used for time discretization. A constant time step of 10^{-3} sec was used in all simulations. The SIMPLEC algorithm was used for velocity-pressure coupling. Coarse mesh simulations were first run at steady state until the sum of the normalized absolute residuals converged to reasonably low values (10^{-3} – 10^{-4}). The converged results then were used as initial conditions for the unsteady simulations, which were run for several flow-through times until periodicity in the flow was observed. Medium and fine mesh simulations were started from interpolated coarse and medium mesh solutions, respectively. Sufficient convergence at each time step was assumed to have been reached when the sum of the normalized absolute residuals was less than 10^{-6} for energy and 10^{-4} for all other variables.

The simulations were performed for the set of cross-draft velocity (V_{cross}) and face velocity (V_{face}) combinations given in Table I. The face velocities (V_{face}) given in the table were

TABLE I. Airflow Velocities Used in the Simulations

Case	V_{cross} (m/sec)	V_{face} (m/sec)	V_{cross}/V_{face}
A	0.073	0.999	0.073
B	0.073	0.852	0.086
C	0.073	0.691	0.106
D	0.073	0.550	0.133
E	0.182	0.981	0.186
F	0.291	0.969	0.300
G	0.291	0.526	0.553

estimated from the mass balance between the hood face and the hood exhaust where a velocity outlet boundary condition was imposed. The table also lists a set of letters assigned to each case and V_{cross}/V_{face} values to be used hereafter. Based on the shoulder diameter of the mannequin ($D_s = 0.45$ m) and the approaching velocity of the air at 297 K, the Reynolds number (Re) was in the range of about 4500–13,700. Based on the temperature differences and airflow velocities, the Richardson number ($Ri = Gr/Re^2$), which is a measure of relative strength of natural convection with respect to forced convection, ranged from 2.22 to 20.87 (Table II). Gravitational force was always included in the simulations.

RESULTS AND DISCUSSION

For the aforementioned conditions, a series of simulations were performed for four different cases. In the first and second cases, the focus was on the effects of each cross-draft's strength and direction, respectively. These simulations were performed under isothermal conditions. In the third and fourth cases, the effects of a worker's body heat and body shape on the flow and concentration fields, respectively, were investigated. In the simulations of the first three cases, the simple rounded mannequin was used, and in the fourth case the humanoid mannequin was employed. While the results from all simulated conditions were used for trend analysis, the temperature and the velocity fields were presented only for the conditions listed in Table III.

TABLE II. Richardson Number (Ri) for the Cases Investigated

Case	V_{cross}/V_{face}	Ri
A	0.073	14.5
B	0.086	16.3
C	0.106	18.3
D	0.133	20.9
E	0.186	4.06
F	0.300	2.22
G	0.553	2.94

TABLE III. Cases and Their Explanations

Case	Explanation
A	Low V_{cross}, High V_{face}
D	Low V_{cross}, Low V_{face}
F	High V_{cross}, High V_{face}
G	High V_{cross}, Low V_{face}

Effect of the Cross-Draft (V_{cross})

In this part of the study the flow simulations were limited to isothermal conditions (i.e., the worker's body heat was not included in the calculations). The air, mannequin, and all walls were at the same temperature (297 K). Figure 3 shows the trend of the estimated and measured concentrations as a function of the V_{cross}/V_{face} ratio at the nose (Point 1) and mouth (Point 2) of the simple rounded mannequin. In the figure it can be seen that the exposure level generally increases with increasing values of V_{cross}/V_{face} until a critical value is reached. For levels of V_{cross}/V_{face} greater than this critical ratio concentrations begin to decrease. However, a closer look at the figure reveals that the concentrations are sensitive to the mesh resolution and that the coarse mesh computations are not able to correctly estimate the critical V_{cross}/V_{face} ratio. However, with increasing mesh resolutions, the estimation curve shifts to the right and gradually approaches the correct V_{cross}/V_{face} for the peak concentrations found in the exposure experiments.

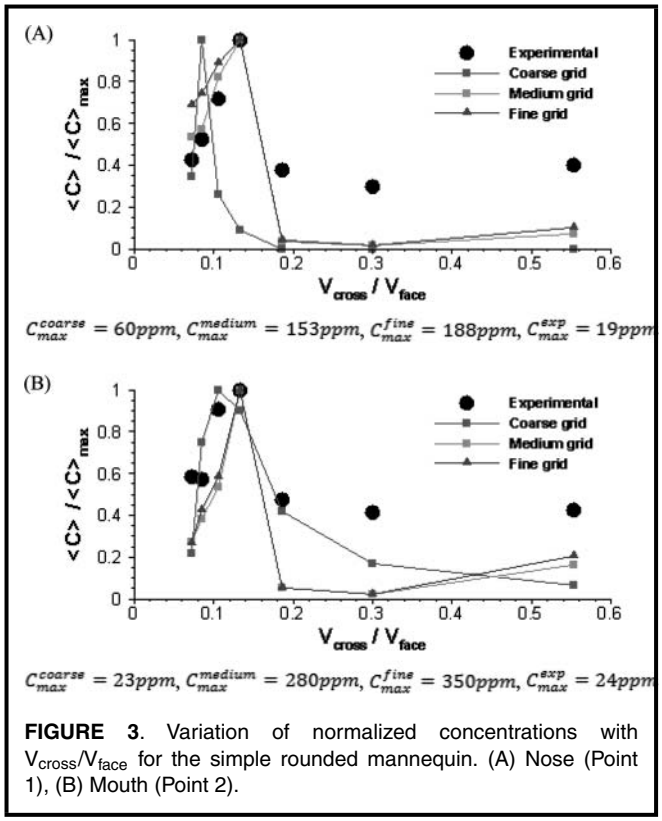

FIGURE 3. Variation of normalized concentrations with V_{cross}/V_{face} for the simple rounded mannequin. (A) Nose (Point 1), (B) Mouth (Point 2).

Although the mesh dependency of the concentrations in the breathing zone is clear, in the non-critical regions (e.g., near the center of the hood enclosure) the mesh convergences were somewhat better for both concentration and velocity. This behavior indicates that nonlinear interactions of mesh size, turbulence model, and numerical scheme may play an important role in the accurate estimation of the flow field and concentration levels in the mannequin's breathing zone. The experimental and simulated conditions could not be matched exactly, a result of the discrepancy between the estimated and measured concentration values. Therefore, in the rest of the study, the focus was placed more on the qualitative than quantitative analyses. The results from the fine mesh computations are presented due to the good qualitative agreement observed in Figure 3.

Online Figure S4 illustrates the estimated time-averaged stream-traces and the snapshot taken during the experiments. It is clear from the figure that there are vortical flow structures in front of the mannequin. These vortical structures arise from the bluff body effect of the mannequin. They are captured well in the simulations. The vortices shown in the figure are indicative of highly turbulent mixing near the hood face.

The size and location of the observed vortices vary from case to case. For example, at high V_{cross} and low V_{face} values (see Case G in Figure 4) the smaller vortices are slightly displaced in the direction of the cross-draft, whereas at low V_{cross} and low V_{face} levels (Case D) the suction force seems to dominate the cross-draft, leading to a relatively more symmetric distribution of both the flow and concentration fields. On the whole, for this configuration, the location of vortices depends on the relative strengths of the competing air currents (i.e., the cross-draft and face velocity).

Figure 5 depicts the flow pattern and the concentration distribution on a transverse plane at the mannequin's shoulder height. Inspection of Figure 5 suggests that when the hood's suction force and the cross-draft are comparable (A) or when the hood's suction force dominates the cross-draft (B), the flow inside the hood tends to be more symmetric, including the two large recirculation zones attached to the side walls of the hood. However, when the effect of cross-draft prevails over the hood's suction force (C and D), the size of the recirculation zone attached to the hood's wall on the upstream side of the cross-draft increases and the recirculation zone attached to the hood's wall on the downstream of the cross-draft diminishes. The concentration contours also show how the concentrations are trapped within the recirculation zones near the hood's wall on the upstream side of the cross-draft. Interestingly, Figure 5 also reveals that there is no significant flow separation around the mannequin's torso and, hence, no recirculation zone extending into the hood. It seems that the acceleration of the flow into the hood hinders flow separation around the mannequin and, thus, the formation of recirculation zones.

Another feature seen in Figure 5 is that compared to the generally high concentrations near the walls, the central region of the hood face remains relatively free of contaminants. Although the exact location of the boundaries of the central region may change from one case to another, it is clear that this region is slightly wider than the mannequin's torso and covers the upper torso and the breathing zone near the face. The reason for this favorable situation is that the clean ambient air converging to the hood enters the hood through the central region and is streamlined toward the back of the hood, thereby minimizing the mixing of contaminants near the hood walls. The smoke trace in online Figure S5 shows the streamlining of the clean air toward the back of the hood and the lack of mixing with the contaminated areas, at least near the hood face.

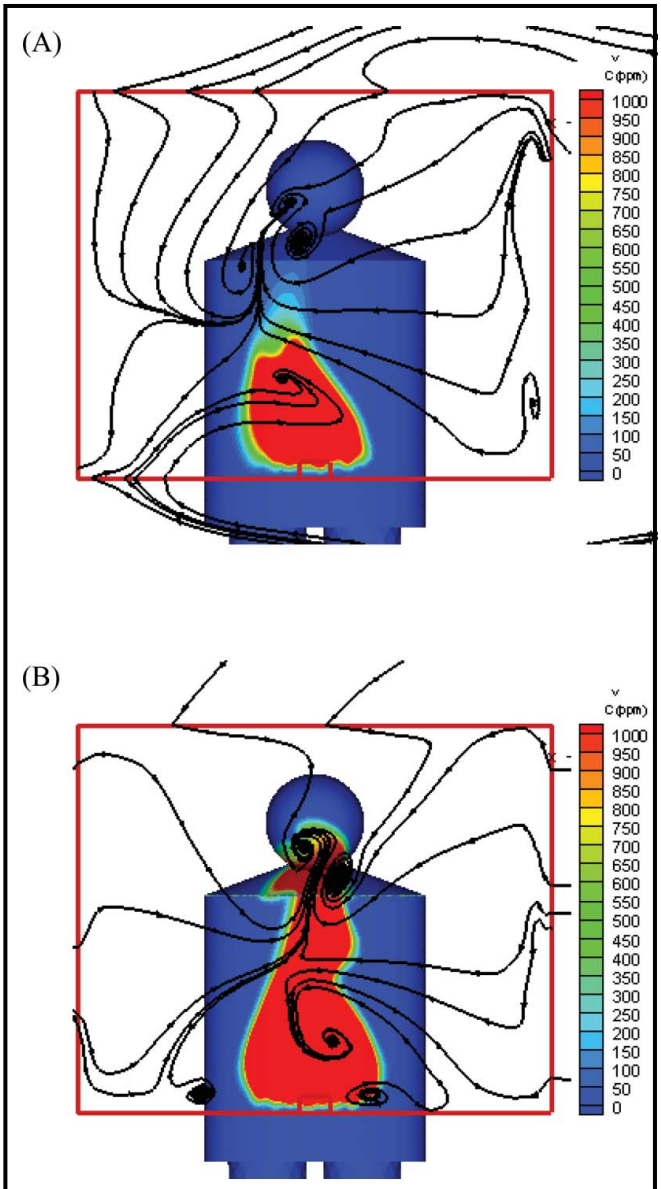

FIGURE 4. Vortices in front of the simple rounded mannequin and their displacement under the effect of cross-draft. (A) High V_{cross} (Case G), (B) Low V_{cross} (Case D).

Figure 6 illustrates the average flow and concentration patterns on the mid-sagittal plane. Again, there is no indication that the presence of the mannequin induces recirculating flow in its breathing zone. The stream-traces make it clear that the vortices seen at the shoulder level are drawn directly toward

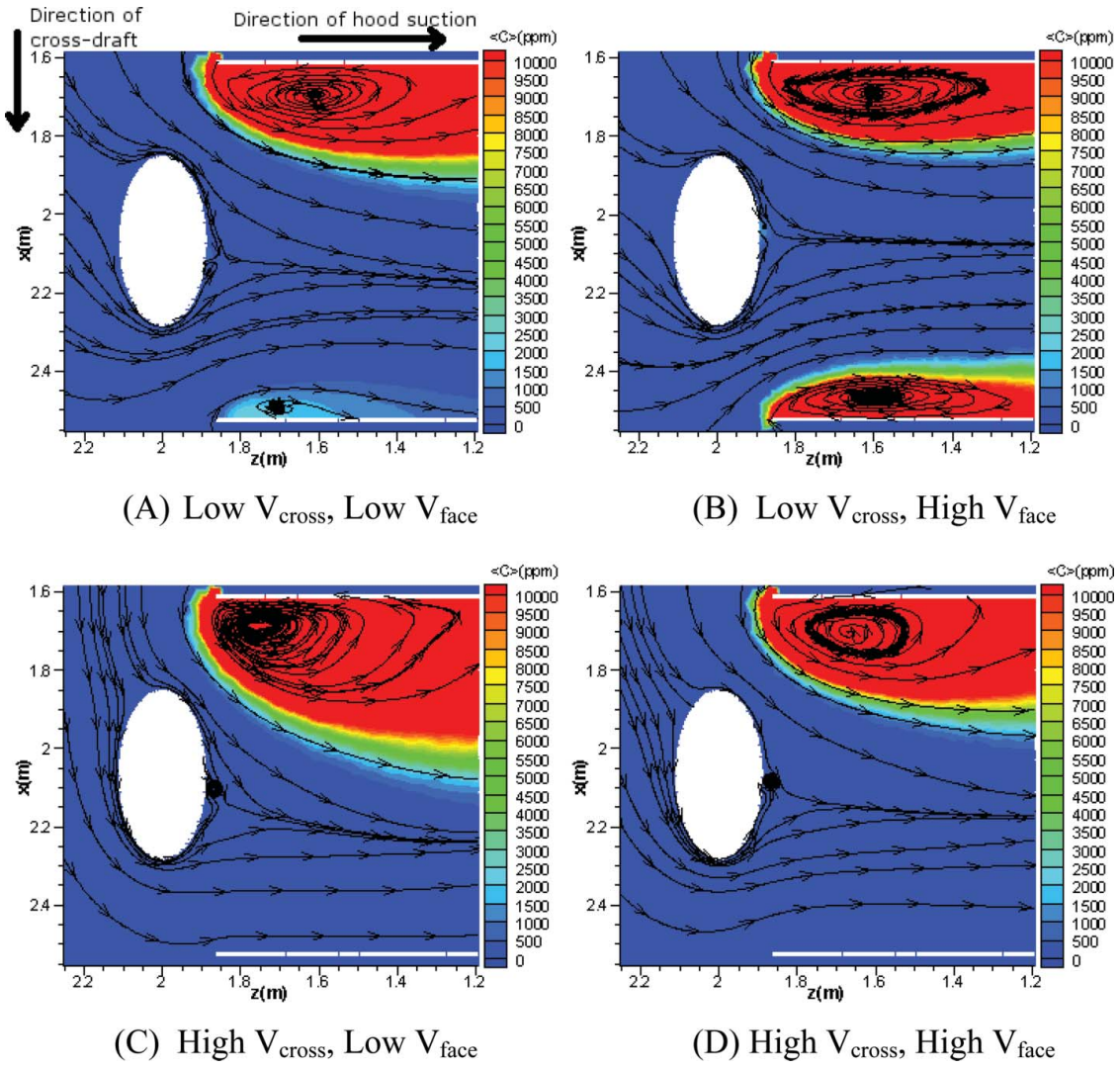

FIGURE 5. Airflow flow patterns and concentration fields on a transverse plane at the waist level of the simple rounded mannequin. (A) Case D, (B) Case A, (C) Case G, (D) Case F.

the back of the hood under the effect of suction. Furthermore, an upward flow right in front of the worker is seen, as is the large vortical motion on the work surface. The snapshot of the smoke shown in online Figure S6 confirms the presence of the large vortex captured in the simulations. The upward flow of air seems to be the major mechanism that carries the contaminants from the source to the worker's breathing zone.

The contours of longtime-averaged concentration on the surface of the worker's body are plotted in Figure 7 using an adjusted color scale. At higher cross-draft velocities (Cases G and F) the concentrations in the breathing zone of the mannequin are lower than the values at lower cross-draft velocities. The concentration changes considerably over the area of mannequin's face. That finding raises the following important issues: (*i*) the concentration at a given monitoring/sampling location may vary depending on the worker's posture, (*ii*) the exact locations of sampling probes may be important, and (*iii*) exposures may be sensitive to small changes in the movement and position of the worker's head. Investigation of these issues is beyond the scope of the present study.

Although no major flow separation around the mannequin was found in front of the mannequin, flow separation and eddy formation was captured at the edges of the hood face (online Figure S7). The flow entering the hood separated at the top and bottom edge of the hood face and formed large eddies that moved toward the back of the hood under the effects of the suction force. The formation and tumbling of these eddies can be expected to augment the unsteady behavior of the vortices present in front of the mannequin.

The time history of the velocity component perpendicular to the hood face for Case A is shown in (A) of online Figure S8. It is clear that the motion was periodically unsteady in front of the mannequin. The unsteadiness in the flow caused variability in the instantaneous concentration levels. This is demonstrated in (B), where the time history of concentration at the nose (Point 1) is presented. As can be seen in the

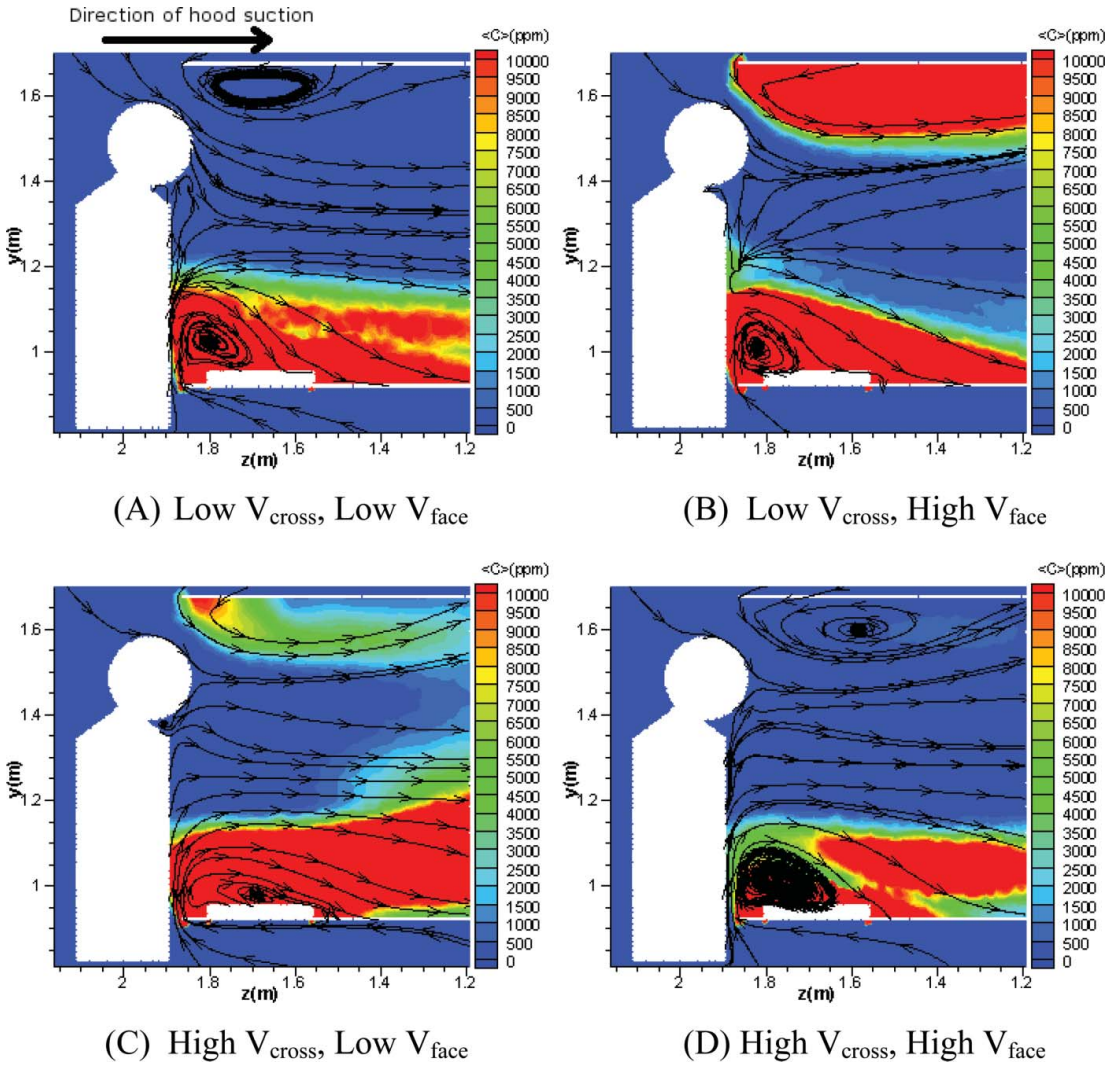

FIGURE 6. Airflow patterns and concentration fields on the mid-sagittal plane of the simple rounded mannequin. (A) Case D, (B) Case A, (C) Case G, (D) Case F.

figure, the instantaneous values of the concentration varied up to 50% of its mean value even under isolated simulation conditions. In an actual work place, the nonlinear interactions of the various extraneous factors would augment the variability both in magnitude and in frequency. The power spectral density diagrams obtained by Fourier-transform of velocity and concentration series from Case A clearly indicate that there were two dominant frequencies (1.35 Hz and 2.7 Hz) associated with the large-scale instabilities in front of the mannequin's head. These frequencies changed depending on the air velocities. In general, at higher suction rates (Cases A, E, and F) the frequencies reached higher values, indicating presence of smaller-scale strong instabilities.

Effect of Direction of Draft

To investigate the effect of draft direction on the wake flow, a simulation for Case D was performed for a flow configuration where the draft was directed toward the simple, rounded mannequin's back. The estimated time-averaged flow field around the mannequin is illustrated in Figure 8. Notably, for this flow configuration, a recirculation zone induced by the flow separation around the mannequin was captured. This indicates that unlike the side-draft, which inhibited the formation of lateral vortices (Figure 5), the draft coming from the mannequin's back helps form lateral vortices. In principle, these vortices are indicators that there is high mixing induced by shear turbulence in front of the mannequin. Therefore, these vortices can draw contaminants from elsewhere in the hood toward the worker's breathing zone. Over time, this may lead to accumulation of contaminant and thus to higher levels of exposure. From this point of view, the flow from the back configuration seems to be a more severe case than the case with the side-draft.

Effect of Body Heat

In an attempt to investigate the worker's thermal impact on the airflow and exposure, the simulations were repeated,

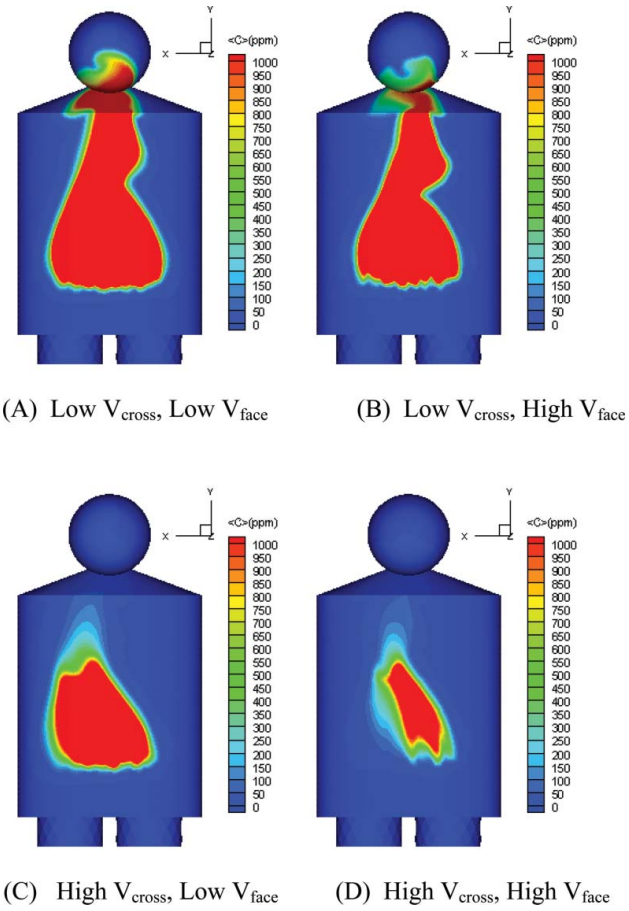

FIGURE 7. Concentration distributions on the surface of the simple rounded mannequin (A) Case D, (B) Case A, (C) Case G, (D) Case F.

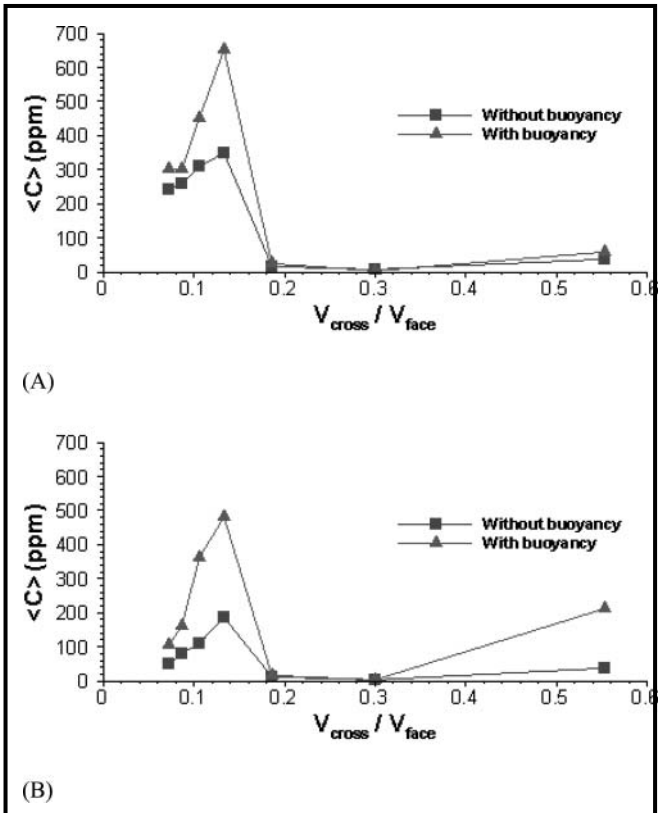

FIGURE 9. Effect of buoyancy on the estimated average concentrations for Cases A–G with simple rounded mannequin. (A) Nose (Point 1), (B) Mouth (Point 2).

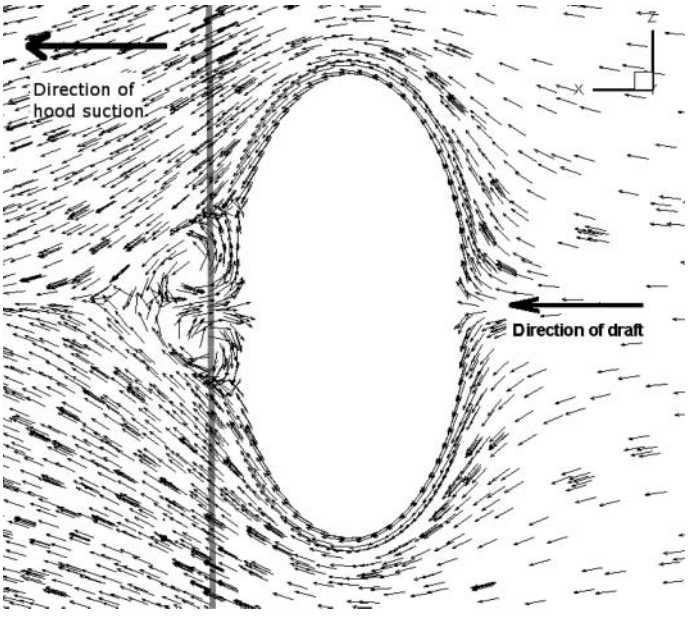

FIGURE 8. Flow pattern around the simple rounded mannequin.

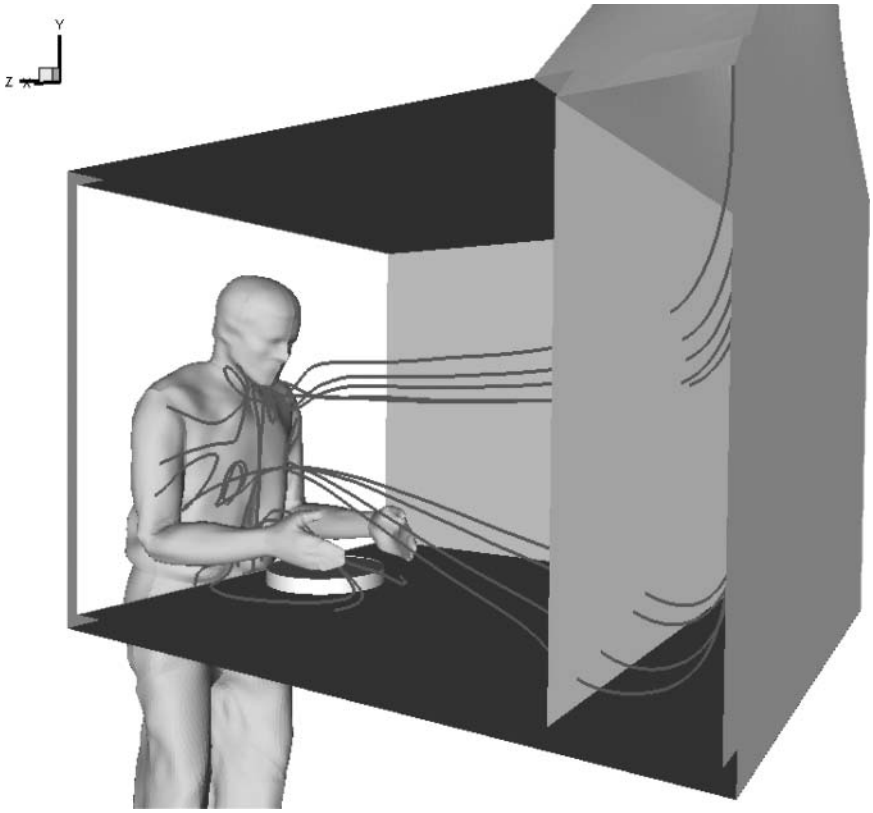

FIGURE 10. Stream-traces in front of the humanoid for Case D.

this time taking the worker's body heat into account. Figure 9 illustrates the effect of buoyancy on the exposure levels at the nose (Point 1) and the mouth (Point 2) of the simple rounded mannequin for different V_{cross}/V_{face} values. It is evident from the figure that the exposure trends with the heated mannequin are similar to those estimated with the unheated mannequin (isothermal case). However, buoyancy had a notably negative (causing an increase) influence on the exposure level when the cross-drafts were weak (Cases A–D). Especially for Case D, where the lowest flow rates were used, the exposure levels increased about 150% due to the buoyancy effects. On the other hand, at higher V_{cross}/V_{face} values (Cases E–G) where the cross-draft convection dominated the suction force, buoyancy effects were negligible. An exception seems to have occurred at the mouth (Point 2) when V_{cross}/V_{face} value was about 0.553 (Case G). This might be attributed to localized flow structures resulting from interactions of body heat, cross-draft, and suction force.

Online Figure S9 shows the temperature and flow field for Case D on the mid-sagittal plane. The heat released from the worker's body did not penetrate into the recirculation zone right above the work surface. Consequently, it did not have much impact on the transport of the contaminant near the source resting on that surface. However, outside the recirculation zone, such as at the levels of the shoulder and head, the heat transfer was relatively more pronounced due to the higher values of the Grashof number. Nevertheless, unlike the significant changes in the flow patterns seen in quiescent or low wind-speed environments without exhaust hoods, buoyancy did not cause major changes in the flow pattern. Instead, at weak cross-drafts, it just enhanced the upward flow and changed the frequencies of flow oscillations in front of the mannequin.

Online Figure S10 demonstrates the impact of buoyancy on the Reynolds-averaged velocity near the nose for Case D, for which the exposure level was most affected by buoyancy effects. The figure reveals that at low airflow rates, the effect of buoyancy manifested through the introduction of low frequency motions to the airflow.

Effect of Body Shape

This part of the study presents the results obtained with the humanoid mannequin and the velocity ratio (V_{cross}/V_{face}) used in case D. Figure 10 illustrates the stream-traces in the wake of the humanoid. It is clear that vortical motions, similar to the ones seen with simple rounded mannequin (Figures 4 and S4), were present. Figure 11 illustrates the flow field on transverse planes at the waist and the chest levels of the humanoid. Although the wake flow was asymmetric due to the side-draft, there was no major flow separation as was found in the case with the simple rounded mannequin (Figures 4 and S4).

Online Figure S11 shows the estimated flow and concentration fields at the hood face. The figure indicates that while

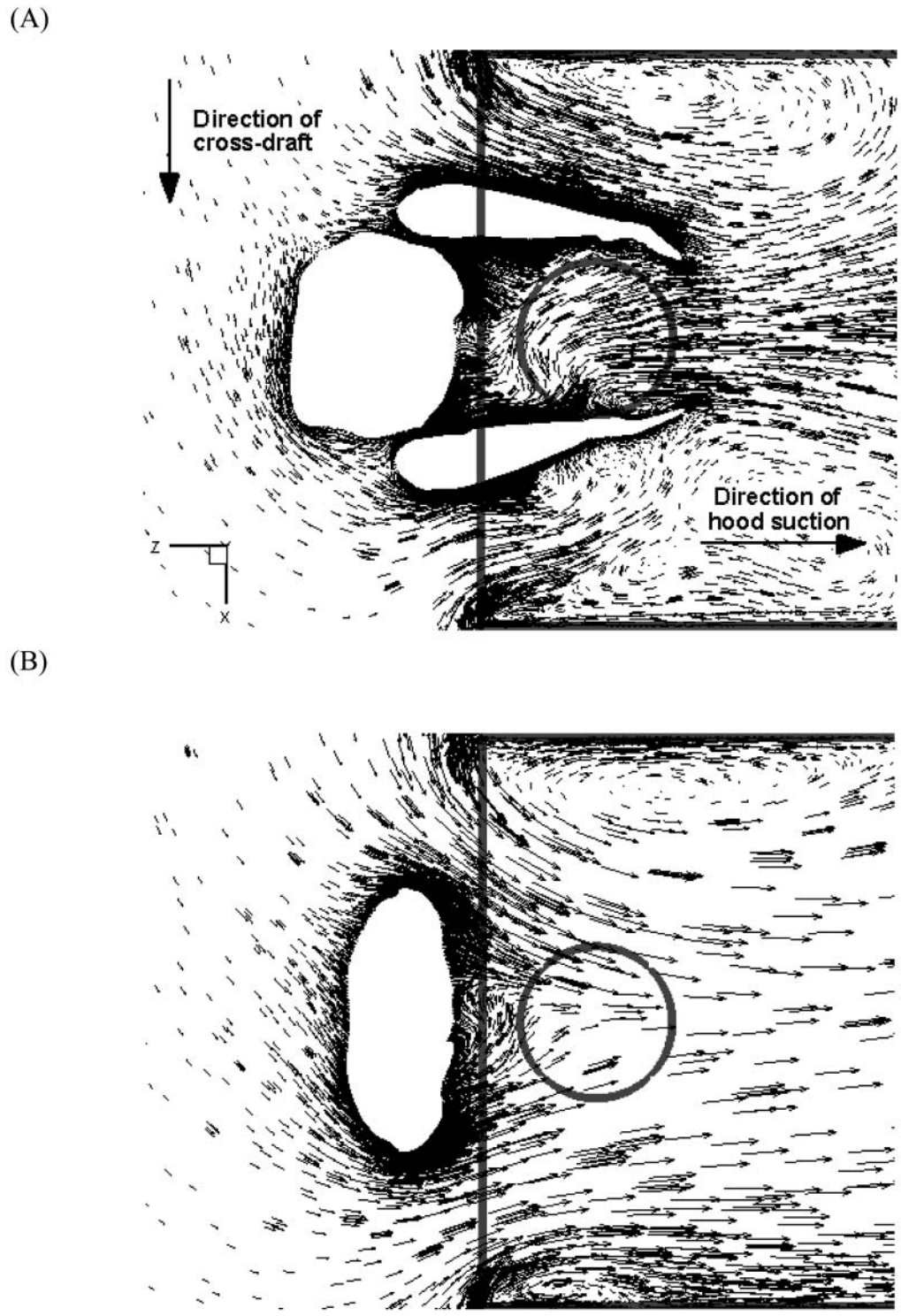

FIGURE 11. Estimated velocity pattern around the humanoid for Case D. (A) Waist height, (B) chest height. Solid lines indicate the boundaries of the hood and the position of the contaminant source.

the vortical motion seen at the shoulder level of the simple mannequin were present, the large vortex seen at the waist level of the simple rounded mannequin (Figure 4B) apparently was prevented due to the humanoid's posture and its arms reaching into the hood. Nevertheless, from the concentration contours given in Online Figure S11, one can see that the contaminant was transported to the humanoid's breathing zone, as was the case of for the simple mannequin (Figures 4B and 7A). This

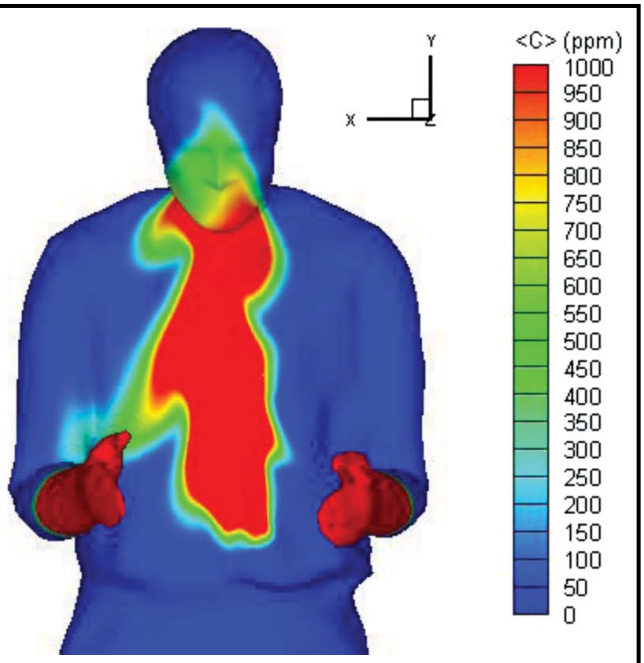

FIGURE 12. Estimated concentration distribution on the surface of the humanoid for Case D.

implies that for the conditions considered here, the stationary arms of the humanoid mannequin had negligible influence on the transport of contaminants from within the hood to the breathing zone. Human workers' arm movements can enhance the turbulence mixing, which in turn may lead to higher levels of exposure to contaminants.

Figure 12 shows the concentration distribution on the surface of the humanoid mannequin. It is seen that the high concentrations of the contaminant were confined mostly to under the chin. This indicates that the humanoid's chin lessens the transport of gaseous contaminants to its face. On the other hand, due to the smooth and spherical representation of the simple mannequin's head, high concentrations covered a wider region on its face (Figure 7A). These estimations may suggest that for workers with the same heights, those with greater chin prominences may experience lower levels of exposure to gaseous contaminants. However, the situation may vary for workers with different body heights. Specifically, shorter workers might be exposed to higher level of contaminants under the same conditions because they would be closer to the contaminant source that is located on the work surface of the hood. Finally, a shorter or longer neck may be critical in the level of exposure to contaminants. A worker with a long neck could be exposed to less contaminant than a worker with a shorter neck.

CONCLUSION

Effects of extraneous factors on the flow dynamics and associated contaminant transport—in the near wake of a worker standing in front of an industrial-type benchtop enclosing hood—were investigated. The extraneous factors considered were relative strength of cross-draft with respect to suction by the hood, direction of draft, and the worker's body heat and shape.

Over the range of side-draft cases studied, it was found that a side-draft stronger than the suction force created by the hood may reduce the exposure level by removing much of the contaminant from the breathing zone. On the other hand, for a weak side-draft, stronger suction was required to minimize the exposure level. As for the flow structures in the side-draft case, the simulations captured the unsteady vortical motions induced by the bluff body effect of the worker's body. The estimated flow structures and concentration trends, in general, were in good agreement with the concurrent experiments. However, the estimated quantitative results in the breathing zone were sensitive to the mesh resolution.

When the draft came from the worker's back, the numerical simulations indicated that lateral vortices were present in the worker's wake. Therefore, this particular configuration was more severe than the side-draft cases since the lateral vortices could draw contaminants from within the hood into the breathing zone, thus leading to higher levels of exposure to contaminants.

The effect of the worker's body heat on the wake flow dynamics and the breathing zone concentration was negligible for strong side-drafts. However, for weak side-drafts the worker's body heat enhanced the upward flow in front of his torso. The upward flow is capable of perturbing the wake flow. The estimated concentrations revealed that small perturbations to the wake flow can lead to remarkably negative influence (causing an increase) on the exposure level. Therefore, results from isothermal simulations of similar low-speed flows may be misleading in that the associated contaminant transport might be underestimated.

Comparison of the numerical results obtained with the simple rounded body and the anthropometric, complex body (humanoid) revealed that the simple rounded body is a fair representation of the humanoid and thus, presumably, humans. It was also found that the worker's chin lessens the exposure level to some extent. Workers with a longer neck may be exposed to relatively low concentrations. The stationary arms of the humanoid mannequin, which were extended into the hood, seem to have negligible influence on the transport of contaminants to the breathing zone. However, the simple rounded mannequin should be tested with and without arms extended into the hood to verify this assertion. Furthermore, in real work, a worker's movement could be one of the most important factors affecting the level of exposure.

ACKNOWLEDGMENT

The authors are grateful to the National Institute for Occupational Safety and Health (NIOSH) for its support of this research (1 R01 OH008165 Enclosing Hood Effectiveness).

REFERENCES

1. **Altemose, B.A., M.R. Flynn, and J. Sprankle:** Application of a tracer gas challenge with a human subject to investigate factors affecting the performance of laboratory fume hoods. *Am. Ind. Hyg. Assoc. J. 59*:321–327 (1998).
2. **Chern, M.-J., and W.-Y. Cheng:** Numerical investigation of turbulent diffusion in push-pull and exhaust fume cupboards. *Ann. Occup. Hyg. 51*(*6*):517–531 (2007).
3. **Huang, R.F., Y.D. Wu, H.D. Chen, et al.:** Development and evaluation of an air-curtain fume cabinet with considerations of its aerodynamics. *Ann. Occup. Hyg. 51*(*2*):189–206 (2006).
4. **Ljungqvist, B.:** Air movements—The dispersion of pollutants: Studies with visual illustrative methods. *ASHRAE Trans. 93*(*1*):1304–1317 (1987).
5. **Ljungqvist, B.:** Aerodynamic design of fume cupboards. *Saf. Health Pract. 9*:36–40 (1991).
6. **Tseng, L.C., R.F. Huang, C.C. Chen, and C.-P. Chang:** Correlation between airflow patterns and performance of a laboratory fume hood. *J. Occup. Environ. Hyg. 3*:694–706 (2006).
7. **Karaismail, E., and I. Celik:** On the inconsistencies related to prediction of flow into an enclosing hood obstructed by a worker. *J. Occup. Environ. Hyg. 7*:315–325 (2010).
8. **American National Standards Institute (ANSI), American Industrial Hygiene Association (AIHA):** *ANSI/AIHA Laboratory Ventilation Standard* (Z9.5). [Standard] Fairfax, Va.: AIHA, 2003.
9. **Burgess, W., M. Ellenbecker, and R. Treitman:** *Ventilation for Control of the Work Environment*. Hoboken, N.J.: John Wiley & Sons, Inc., 2004.
10. **Zhivov, A.M., L.L. Christianson, and G.L. Riskowski:** Influence of Space Air Movement on Hood Performance. ASHRAE Research Project RP-744. Atlanta, Ga.: ASHRAE, 1995.
11. **Craven, B.A., and G.S. Settles:** A computational and experimental investigation of the human thermal plume. *J. Fluid Eng. 128*:1251–1258 (2006).
12. **Gowadia, H., and G. Settles:** The natural sampling of airborne trace signals from explosives concealed upon the human body. *J. Forensic Sci. 46*(*6*):1324–1331 (2001).
13. **Clark, R.P., and E.C. Edholm:** *Man and His Thermal Environment*. London, U.K.: E. Arnold Ltd., 1985.
14. **Murakami S., S. Kato, and J. Zeng:** Combined simulation of airflow, radiation and moisture transport for heat release from a human body. *Build. Environ. 35*(*6*):489–500 (2000).
15. **Murakami, S.:** Analysis and design of micro-climate around the human body with respiration by CFD. *Indoor Air 14*(*Suppl 7*):144–156 (2004).
16. **Lewis, H.E., A.R. Foster, B.J. Mullan, R.N. Cox, and R.P. Clark:** Aerodynamics of the human microenvironment. *Lancet 293*(*7609*):1273–1277 (1969).
17. **Heist, D., A. Eisner, W. Mitchell, and R. Wiener:** Airflow around a child-size manikin in a low-speed wind environment. *Aerosol Sci. Technol. 37*(*4*):303–314 (2003).
18. **Li, J., I. Yavuz, I. Celik, and S. Guffey:** A numerical study of worker exposure to a gaseous contaminant: Variations on body shape and scalar transport model. *J. Occup. Environ. Hyg. 2*:323–334 (2005).
19. **He, X.:** "Effects of Face Velocity, Cross-Draft Velocity and Interventions on the Performance of a Benchtop Enclosing Hood." Master's thesis, College of Engineering and Mineral Resources, West Virginia University, Morgantown, W. Va., 2010.
20. **Lam, S.H.:** On the RNG theory of turbulence. *Phys. Fluids A 4*:1007–1017 (1992).
21. **Yakhot, V., S.A. Orszag, S. Thangam, T.B. Gatski, and C.G. Speziale:** Development of turbulence models for shear flows by a double expansion technique. *Physics Fluids A. 4*:1510–1520 (1992).
22. **Afshar, R., and S.C. Saxena:** Transport properties of Freon-152a and Freon-142b in the temperature range of 280–510 K. *Int. J. Thermophy. 1*(*l*):51–59 (1980).